Identifying Promising Metal−Organic Frameworks for Heterogeneous Catalysis via High-Throughput Periodic Density Functional Theory

Andrew S. Rosen, Justin M. Notestein, Randall Q. Snurr

Department of Chemical and Biological Engineering, Northwestern University, Evanston,
Illinois 60208, United States

Corresponding authors:

E-mail: j-notestein@northwestern.edu. Tel.: 847-491-5357

E-mail: snurr@northwestern.edu. Tel.: 847-467-2977

Abstract

Metal−organic frameworks (MOFs) are a class of nanoporous materials with highly tunable structures in terms of both chemical composition and topology. Due to their tunable nature, high-throughput computational screening is a particularly appealing method to reduce the time-to-discovery of MOFs with desirable physical and chemical properties. In this work, a fully automated, high-throughput periodic density functional theory (DFT) workflow for screening promising MOF candidates was developed and benchmarked, with a specific focus on applications in catalysis. As a proof-of-concept, we use the high-throughput workflow to screen MOFs containing open metal sites from the Computation-Ready, Experimental MOF database for the oxidative C-H bond activation of methane. The results from the screening process suggest that, despite the strong C-H bond strength of methane, the main challenge is identifying MOFs with open metal sites that can be readily oxidized at moderate reaction conditions.

Keywords: Metal−organic frameworks; high-throughput screening, density functional theory; computational catalysis; methane activation

This is the author manuscript accepted for publication and has undergone full peer review but has not been through the copyediting, typesetting, pagination and proofreading process, which may lead to differences between this version and the Version of Record. Please cite this article as doi: 10.1002/jcc.25787

1. Introduction

With the advent of materials informatics toolkits and software enabling the development of high-throughput (HT) screening workflows,[1–6] HT periodic density functional theory (DFT) has been used to construct databases of electronic, energetic, and structural properties for hundreds of thousands of inorganic materials from first-principles calculations.[7–13] Metal−organic frameworks (MOFs), a novel class of highly porous crystalline materials, are well-suited for computational screening studies due to the modular nature of their inorganic nodes and organic linkers.[14] To date, there are tens of thousands of experimentally synthesized MOFs,[15] and numerous crystal structure databases have been developed from both known[15–17] and hypothetical[14,18] MOF structures.

HT screening of these databases is particularly appealing, as it allows for a greater number of MOFs to be investigated than would be possible experimentally. One of the main goals of HT screening of MOF crystal structure databases is to reduce the time-to-discovery of MOFs with desired chemical and physical properties. In the area of gas storage and separations, HT grand canonical Monte Carlo simulations using classical force fields have been successfully used to identify top-performing MOFs with respect to CH_4 storage capacity,[14] CO_2 capture,[19] H_2 storage,[20] and O_2 uptake.[21] However, extending HT screening of MOFs to applications requiring quantum chemical calculations, such as catalysis, remains a challenge.

Due in part to the large unit cells of many MOFs, the most common approach when modeling MOFs for any catalytic reaction is to crop and terminate the periodic structure to create a finite-sized cluster model of the proposed active site, often consisting of no more than a few dozen atoms.[22] An appropriate choice of where to artificially terminate the MOF unit cell is often not immediately obvious, and this approach is therefore not amenable to HT screening of MOFs with widely varying topologies. Finite cluster models also inherently introduce artificial boundary effects that have the potential to influence charge delocalization[23] and pore-based confinement effects.[24,25] The use of periodic DFT to represent the full crystallographic unit cell naturally resolves these issues, and most implementations of periodic DFT are well-suited for massively parallel calculations that can be used to treat the larger number of atoms in each simulation. Nevertheless, to the best of our knowledge, there has never been a fully automated, HT periodic DFT screening study for any catalytic reaction using MOFs.

In this work, we have developed a HT workflow based on periodic DFT to screen large numbers of MOFs for promising catalytic candidates. As a proof-of-concept, we use this HT workflow to screen MOFs with coordinatively unsaturated metal sites, also known as open metal sites (OMSs), for oxidative C-H bond activation. Due to the large economic demand for a catalyst that can directly convert methane to methanol[26] and motivated by prior work involving MOFs for methane conversion,[27–32] we specifically consider the partial oxidation of methane as the reaction of interest. In the process, we demonstrate the feasibility of a HT-DFT screening workflow for MOF catalysis and make several recommendations for future work involving HT-DFT screening studies of MOFs.

2. General Scheme

Motivated by similar schemes for computational catalysis screening of bulk metals and alloys,[33,34] the general approach for HT-DFT of MOF catalysts can be outlined as follows:

(1) Determine a set of catalytic descriptors that can be used to correlate catalytic activity with readily computed quantities, such as those based on adsorption energies, reaction energies, or electronic structure properties.[35–40]
(2) Identify or construct a dataset of MOF crystal structures to study. Tools such as Pymatgen[1,41] and Zeo++[42] can be used to select MOFs with specific metals, coordination environments, and pore sizes relevant to the given reaction of interest.
(3) Using DFT, optimize the unit cell volume, unit cell shape, and internal degrees of freedom (i.e. atomic positions) for each MOF.
(4) Starting from the optimized MOF structures, initialize the positions of atomic and molecular adsorbates required to predict catalytic activity via (1).
(5) Using DFT, relax the atomic positions of the structures generated via (4).
(6) Compute the catalytic descriptors of interest to rank MOF candidates.
(7) For promising MOF candidates, generate the potential energy diagram for the proposed mechanism and perform detailed electronic structure analyses to better understand the reaction kinetics.

In the following sections, we describe how to fully automate this process when studying MOFs with spatially isolated active sites, given previously determined catalytic descriptors. We then apply this procedure to screen MOFs for the ability to oxidatively activate the C-H bond of methane.

3. Catalytic Descriptors for Oxidative C-H Bond Activation

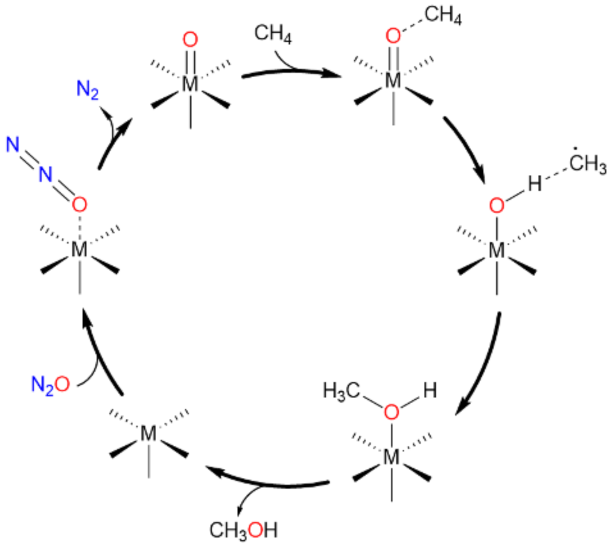

Figure 1. Radical-rebound mechanism for the oxidative C-H bond activation of methane at a coordinatively unsaturated metal site (M) using an N_2O oxidant. The precise coordination environment and M-O bond order are dependent on the given MOF. In this work, we mainly focus on oxidation of the metal center and subsequent H-abstraction.

When studying materials such as MOFs with spatially isolated active sites, the expected mechanism for the conversion of methane to methanol is the radical-rebound mechanism, as shown in Figure 1.[43] For HT screening purposes, we focus on the oxidation of the metal and H-abstraction steps of this mechanism, as they dictate the overall conversion of methane by influencing the number of metal oxide active sites and the activity of each site, respectively. Recently, Nørskov and coworkers have proposed a universal transition state (TS) scaling relationship for the C-H bond activation of methane.[38] This TS scaling relationship can be used to accurately predict the energy of the corresponding TS over a wide range of heterogeneous catalysts based on the strength that an H atom binds to the metal oxide active site, denoted E_{H}. This H-affinity linear scaling relationship has been benchmarked for a wide range of materials, including cation-exchanged zeolites, bulk metal oxides, transition metal surfaces, and MOFs.[38] Here, we define the H-affinity as

$$E_{\mathrm{H}} = E_{\mathrm{MOF-OH}} - E_{\mathrm{MOF-O}} - \frac{1}{2}E_{\mathrm{H_2}} \tag{1}$$

where $E_{\mathrm{MOF-OH}}$ and $E_{\mathrm{MOF-O}}$ are the electronic energies of the metal site with adsorbed OH and O species, respectively, and $E_{\mathrm{H_2}}$ is the electronic energy of H_2. Note that unlike the original description of E_{H},[38] Equation (1) uses H_2 as the H-reference, as justified in the Supporting Information. With this, we can use the universal scaling relationship[38] of

$$E^{*}_{\mathrm{TS,C-H}} = 0.75E_{\mathrm{H}} + 1.96\ \mathrm{eV} \tag{2}$$

to predict the energy of the TS, $E^{*}_{\mathrm{TS,C-H}}$, with respect to the initial oxidized state, as schematically illustrated in Figure S1. With Equations (1) and (2), the C-H bond activation barrier can then be readily computed via

$$E^{*}_{\mathrm{a,C-H}} = E^{*}_{\mathrm{TS,C-H}} - \left[E_{\mathrm{MOF-O-CH_4}} - \left(E_{\mathrm{MOF-O}} + E_{\mathrm{CH_4}}\right)\right] \tag{3}$$

where $E_{\mathrm{MOF-O-CH_4}}$ is the electronic energy of methane adsorbed to the metal oxide active site, and $E_{\mathrm{CH_4}}$ is the electronic energy of gas-phase methane. The asterisks in Equations (2) and (3) are used to denote quantities obtained from a TS scaling relationship rather than directly computed using a TS finding algorithm, although this difference is expected to be no more than ~11 kJ/mol on average based on the work of Nørskov and coworkers.[38]

In contrast with the C-H bond activation step, there is currently no reported universal TS scaling relationship for the step in which the metal site is oxidized. Instead, we consider the extrinsic oxidation reaction energy using N_2O as the proposed oxidant, defined as

$$\Delta E_{\mathrm{ox}} = \left(E_{\mathrm{MOF-O}} + E_{\mathrm{N_2}}\right) - \left(E_{\mathrm{MOF}} + E_{\mathrm{N_2O}}\right) \tag{4}$$

to determine the thermodynamic favorability of oxidation, as has been done in prior work.[38,39] Here, E_{MOF}, $E_{\mathrm{N_2}}$, and $E_{\mathrm{N_2O}}$ are the electronic energies of the bare MOF (i.e. the reduced state), gas-phase N_2, and gas-phase N_2O, respectively. We refer to Equation (4) as an "extrinsic" reaction energy, as the energies for N_2 and N_2O are for the isolated gas-phase species, not in the adsorbed state.

4. Initial Dataset Construction

The starting dataset considered in this work is an 838 MOF subset[44] of the Computation-Ready, Experimental (CoRE) MOF database.[16] The MOFs in this database were originally obtained from the Cambridge Structural Database (CSD) with free and bound solvents removed. The 838 MOFs in this database have previously been optimized at the PBE-D3(BJ) level of theory via the CP2K code,[45] which uses mixed Gaussian and plane-wave basis sets.[46] From this 838 MOF dataset, 168 unique MOFs were selected for analysis based on a high likelihood of having OMSs following optimization and having pore-limiting diameters of at least 3.0 Å as determined by Zeo++[42] (refer to the Supporting Information for full details).

5. Adsorbate Initialization

One of the necessary aspects of any HT screening workflow is that the entire process should be fully automated with minimal user-intervention. For heterogeneous catalysis and other surface science applications, adsorption energies are commonly computed but typically involve the user manually specifying an initial guess for the location of the adsorbate that is later optimized using DFT. This naturally limits the number of materials that can be screened, especially since computational catalysis screening often involves the calculation of numerous adsorption energies per catalytic candidate. In addition, the choice of a good initial location for a given adsorbate can significantly reduce the length of the corresponding geometry optimization by ensuring the structure is relatively close to a minimum in the potential energy surface. We summarize methods to automate this adsorbate initialization process below.

5.1 Vector-Sum Method

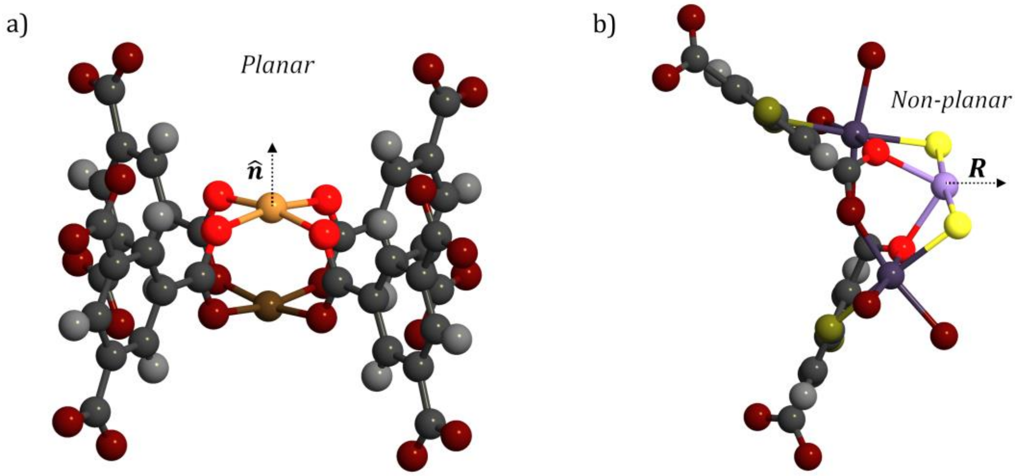

Figure 2. (a) Initializing the position of adsorbates at undercoordinated atoms with planar coordination environments is done in the direction of the unit normal vector to the plane with the fewest neighbors, $\hat{\boldsymbol{n}}$. (b) For non-planar coordination environments, the adsorbate is initialized in the direction resulting from the sum of the normalized distance vectors formed between the coordinating atoms and the central atom, $\boldsymbol{R}$.

An easy-to-implement set of geometrical rules, which we refer to as the vector-sum method, can be used to systematically locate physically relevant adsorption sites on undercoordinated atoms for the purposes of HT-DFT calculations. As an example, consider the chemisorption of a single

O atom to an unsaturated Cu site at the node of the widely studied HKUST-1[47] (Figure 2a). For simplicity, we define the binding site (in this case, a Cu atom) as species $i = 0$, and all atoms in the first coordination sphere are given indices $i = 1$ through n, where n is the coordination number. The proposed metal binding site can be automatically determined using a variety of OMS detection algorithms.[17,42,48] A distance vector, $\boldsymbol{r}_{0,i}$, is then computed for each coordinating atom via

$$\boldsymbol{r}_{0,i} = \boldsymbol{p}_0 - \boldsymbol{p}_i \tag{5}$$

where $\boldsymbol{p}_i$ is the position vector of atom i. Note that $\boldsymbol{r}_{0,i}$ should be the minimum-image distance vector, taking into account the periodicity of the unit cell.

We then determine the planarity of the coordinating atoms via two metrics. The first method involves total least-squares regression of the positions of the coordinating atoms to the equation of a plane, $ax + by + cz + d = 0$. As a second method, we calculate the sum of normalized distance vectors, $\boldsymbol{R}$, as

$$\boldsymbol{R} = \sum_{i=1}^{n} \frac{\boldsymbol{r}_{0,i}}{||\boldsymbol{r}_{0,i}||} \tag{6}$$

We suggest using both metrics as measures of planarity and, through iterative testing, have found that a coordination environment is typically well-described as planar if the root mean square error in the planar fit is less than 0.25 Å or $||\boldsymbol{R}|| < 0.25$ Å.

If the coordination environment is planar, the adsorbate's position $\boldsymbol{p}_{\text{ads}}$ is given by

$$\boldsymbol{p}_{\text{ads}} = \boldsymbol{p}_0 \pm \alpha\hat{\boldsymbol{n}} \tag{7}$$

where $\hat{\boldsymbol{n}}$ is the unit normal vector to the best-fit plane and α is a bond distance scale-factor that is dependent on the proposed adsorbate. For instance, in this work we use $\alpha = 2$ Å for the chemisorption of an O atom to an OMS. To determine the sign in Equation (7), we calculate the number of neighbors within a cutoff distance r_{cut} and choose the direction with fewer neighboring atoms. In this work, we use a value of $r_{\text{cut}} = 2.5$ Å. The choice of sign is important for many MOFs, especially those with paddlewheel secondary building units such as HKUST-1.[47] If the coordination environment is not planar, the desired adsorption site $\boldsymbol{p}_{\text{ads}}$ is given by

$$\boldsymbol{p}_{\text{ads}} = \boldsymbol{p}_0 + \alpha\boldsymbol{R} \tag{8}$$

This approach attempts to maximize the symmetry of the molecular geometry, such as the formation of a trigonal bipyramidal geometry from the original seesaw structure shown in Figure 2b. Naturally, a modified approach is needed for coordination numbers of three or less, which we describe in the Supporting Information along with the method for determining the atoms within the first coordination sphere. While the example shown in Figure 2 is for a monatomic adsorbate, this procedure can be readily extended for the adsorption of small molecules as well.[49]

5.2 Potential Energy Grid Method

To initialize the position of molecular adsorbates, a different method based on a molecular mechanics-based potential energy grid (PEG) generated for each MOF can be used to identify physically plausible adsorbate positions. In this work, we consider the adsorption of CH_4 near the metal oxide active site of each MOF following oxidation of a single metal center. The PEG for each MOF is calculated using a single-site TraPPE[50] CH_4 probe in RASPA[51] with a grid discretization of 0.1 Å in x, y, and z (Figure 3). The lowest energy position within a cutoff distance $r_{\text{cut,PEG}}$ from the proposed active site is taken as the initial position for the adsorbate. Since we used a single-site CH_4 probe, the central C atom was placed at the lowest energy site within $r_{\text{cut,PEG}} = 3.0$ Å, and one of the four H atoms in CH_4 was made colinear with the O atom at the active site and the central C atom of CH_4. The remaining three H atoms are arranged to satisfy the tetrahedral geometry of CH_4.

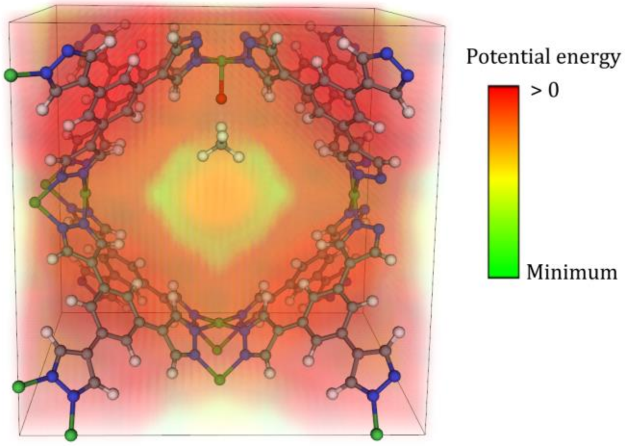

Figure 3. Potential energy grid obtained using a single-site CH_4 probe in an example MOF with a hypothetical $[NiO]^{2+}$ active site. The position of the CH_4 molecule has been initialized in the low-energy adsorption site. The repulsive regions are colored in dark red, and the most attractive region is shown in light green. Color key: Ni (green), O (red), N (blue), C (gray), H (white).

5.3 Implementation of Methods

Additional details regarding the implementation of the adsorbate initialization algorithms used in this study can be found in the Supporting Information. An open-source Python code referred to as the MOF Adsorbate Initializer is made publicly available to readily perform fully automated adsorbate initialization workflows such as those described in this work.[49] This code makes use of Pymatgen[1] and the Atomic Simulation Environment (ASE)[2] to carry out the adsorbate initialization process and has optional interfaces to Zeo++[42] or Open Metal Detector[17,52] for the automated detection of OMSs in MOFs. For PEG-based adsorbate initialization, the code is compatible with multiple volumetric data formats for the energy as a function of (x, y, z) coordinates, including PEGs computed from RASPA[51] or PorousMaterials.jl[53].

6. High-Throughput Density Functional Theory

Given that the unit cells of MOFs can contain hundreds of atoms and that multiple reaction energies and kinetic barriers are needed to predict catalytic activity, it is essential that a robust and efficient HT-DFT workflow is established. In this section, we describe the multi-stage optimization scheme used to successfully perform the calculations in this work (~500 DFT calculations on materials with an average of ~200 atoms per Niggli-reduced unit cell).

6.1 Constant Parameters

All periodic DFT calculations are performed with the Vienna *ab initio* Simulation Package (VASP) v.5.4.1[54,55] and the projector-augmented wave (PAW) pseudopotentials[56] outlined in Table S1 of the Supporting Information. The electron exchange-correlation is described by the Perdew-Burke-Ernzerhof (PBE) functional,[57] and Grimme's D3 dispersion correction[58] with Becke-Johnson (BJ) damping[59] is used to account for van der Waals (vdW) dispersion interactions. We use the PBE functional as a reasonable balance between computational cost and accuracy for the purposes of HT screening.[60,61] Due to the electronically insulating nature of most MOFs, Gaussian smearing of the band occupancies with a small smearing width of σ = 0.01 eV is used prior to extrapolation to the 0 K limit. Transition state calculations are done using an automated procedure involving the climbing image nudged elastic band method[62] and the dimer method[63] as described in the Supporting Information.

6.2 Electronic Optimization

The default electronic optimization algorithm used in this work is a preconditioned conjugate gradient (CG) algorithm (also referred to as the "all bands simultaneous update of orbitals" algorithm), which is suggested for both large and insulating materials.[64,65] An additional benefit of this algorithm is that it is not heavily reliant on the choice of Pulay density mixing parameters,[66] which are used to achieve convergence of the self-consistent field (SCF) but can be highly material-specific.[8,9,54,67] This is in contrast with electronic optimization routines more commonly used for modeling metallic systems (e.g. blocked Davidson, RMM-DIIS),[54] which generally require frequent monitoring of the SCF convergence and *post hoc* tweaking of the mixing parameters to resolve problematic convergence issues in a HT-DFT workflow.[8,9]

6.3 Multi-Stage Geometry Optimizations

6.3.1 Optimizing the Volume of Bare MOFs

As is common in computational catalysis studies, the first step of the HT-DFT workflow involves optimizing the unit cell of each bare MOF, including the cell shape, cell volume, and all internal degrees of freedom. As shown in Figure 4, we performed a multi-step relaxation scheme inspired in part by the one used in constructing the Open Quantum Materials Database (OQMD).[7]

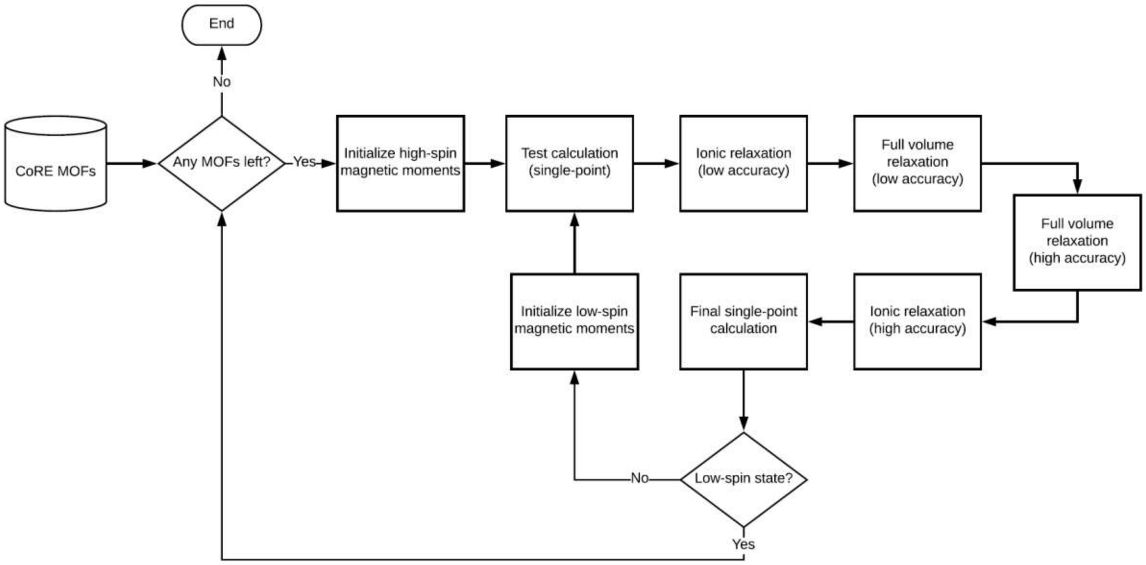

Figure 4. Schematic summarizing the high-throughput periodic density functional theory workflow for performing volume relaxations (including the cell parameters, cell shape, and internal degrees of freedom) of bare MOFs.

In the first step, a test single-point calculation is performed to confirm that there are no VASP-related errors. Any errors in this stage (e.g. too high a degree of parallelization requested for a particularly small MOF) and throughout the workflow (e.g. convergence failures) are fixed on-the-fly using a procedure similar to the Custodian tool of the Materials Project.[8,9] Following the test calculation, a preliminary low-accuracy ionic relaxation is performed (i.e. relaxation of atomic positions at fixed cell shape and volume), which is necessary for the efficient geometry optimization of most MOFs due to the large number of atoms per unit cell. The default maximum plane-wave energy cutoff specified by the pseudopotentials (generally 400 eV) and a k-point grid[68] of 100 k-points per atom (KPPA) are used.

The initial ionic relaxation is done in two main stages. In the first stage, we use the Broyden-Fletcher-Goldfarb-Shanno (BFGS) algorithm with a line search mechanism that ensures the energy and absolute value of the force decrease monotonically. This algorithm is available in ASE[2] and is used until the magnitude of the maximum force, $|F_{\mathrm{max}}|$, is less than 5 eV/Å. Compared to the default CG or quasi-Newton (QN) algorithms in VASP, we found that the BFGS line search algorithm was able to resolve high forces without atoms in the MOF unit cell moving to unphysical locations far away from their starting positions. Once the 5 eV/Å threshold is reached, the CG algorithm in VASP is used until $|F_{\mathrm{max}}| < 0.05$ eV/Å.

Following the low-accuracy ionic relaxation, a full volume relaxation (i.e. cell shape, cell volume, ionic positions) is performed at an initial low-accuracy setting. To prevent Pulay stresses,[69] the plane-wave kinetic energy cutoff is raised to 520 eV. All other parameters are unchanged. In the subsequent high-accuracy volume relaxation, the density of the k-point grid is increased from 100 KPPA to 1000 KPPA, and the force-tolerance is changed to 0.03 eV/Å. A k-point grid density of 1000 KPPA is also currently used in the Materials Project[8] and has been previously used to model MOFs.[60]

A final high-accuracy ionic relaxation is performed after the high-accuracy volume relaxation to confirm that the ionic positions are fully converged when the cell shape is kept fixed, and then a single-point calculation is performed to store the final wavefunction and charge density. Starting from the converged high-spin structure, a low-spin spin-initialization is considered (as discussed in Section 6.4). If performed, the lowest energy structure from the two initialized spin states is used for further stages of the HT screening workflow. The key DFT parameters are summarized in Table 1 (with all parameters listed in Table S2).

Table 1. Periodic DFT parameters used in the optimizing the bare MOFs. ENCUT is the plane-wave kinetic energy cutoff, KPPA is the number of k-points per atom (with the corresponding k-point grids generated using Pymatgen[1]), and $|F_{\mathrm{max}}|$ is the force-convergence criterion.

Stage	ENCUT (eV)	KPPA	$\lvert F_{\mathrm{max}} \rvert$ (eV/Å)
1: Ionic relaxation (low-accuracy)	400	100	0.05
2: Volume relaxation (low-accuracy)	520	100	0.05
3: Volume relaxation (high-accuracy)	520	1000	0.03
4: Ionic relaxation (high-accuracy)	520	1000	0.03
5: Single-point (high-accuracy)	520	1000	N/A

The percent difference in computed cell volumes between the low-accuracy and high-accuracy volume relaxations is shown in Figure 5a. For the vast majority of tested MOFs, the cell volume is nearly identical at the low- and high-accuracy settings. As shown in Figure 5b, the deviation in cell volumes is most pronounced for MOFs with a small number of atoms per unit cell where the increased k-point density is expected to increase the accuracy of the results. While 100 KPPA and 1000 KPPA corresponds to the same k-point grid (consisting of just the Γ-point) for 33% of the MOFs in this analysis, 90% of MOFs had a volume change of less than ±1% when going from the low- to high-accuracy settings. This is consistent with the findings of Ceder and coworkers,[9] who suggested that the plane-wave energy cutoff (rather than the size of the k-point grid) has a more pronounced effect on cell volumes.

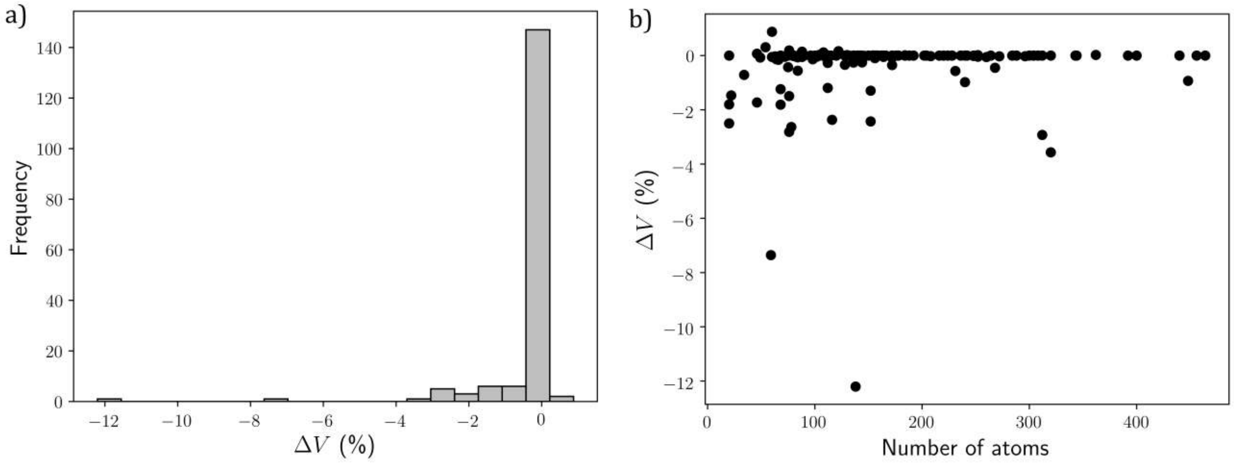

Figure 5. (a) Percent deviation in the cell volume, ΔV, computed with low-accuracy settings (cutoff = 520 eV, KPPA = 100, $|F_{\text{max}}| < 0.05$ eV/Å) compared to high-accuracy settings (cutoff = 520 eV, KPPA = 1000, $|F_{\text{max}}| <$ 0.03 eV/Å), defined as $\Delta V = (V_{\text{high acc.}} - V_{\text{low acc.}})/V_{\text{low acc.}}$. (b) Percent deviation in cell volumes as a function of the number of atoms per Niggli-reduced unit cell. Data shown in this figure is for the high-spin initialization cycle of the high-throughput workflow.

6.3.2 Optimizing the Ionic Positions of MOFs with Adsorbates

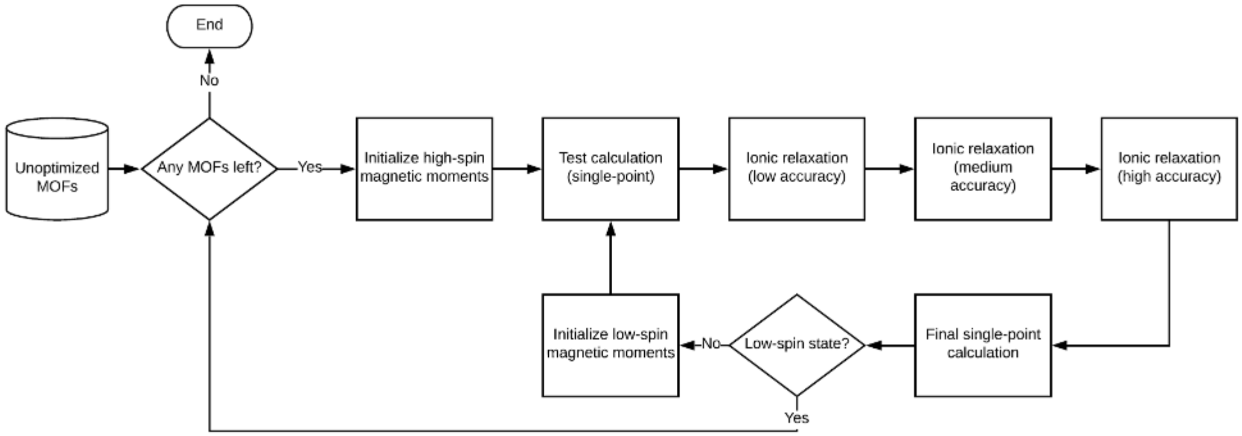

Figure 6. Schematic summarizing the high-throughput periodic density functional theory workflow for performing ionic relaxations (i.e. internal degrees of freedom only) of MOFs with adsorbates.

The multi-stage optimization procedure for relaxing the atomic positions of MOFs with adsorbates (at fixed cell shape and volume) is summarized in Figure 6 and is similar to the procedure for volume relaxations of the bare MOFs. At the medium-accuracy ionic relaxation stage, the k-point density is increased from 100 KPPA to 1000 KPPA, but the default (400 eV) plane-wave kinetic energy cutoff is still used. For both the medium- and high-accuracy ionic relaxations, the Fast Inertial Relaxation Engine (FIRE) algorithm[70] as implemented in VTST Tools[71] is used instead of the CG algorithm for relaxing the ionic positions. This was found to be necessary for optimizing the structures of MOFs with adsorbates, as the atoms far away from the adsorption site are already close to their optimized positions and the PES is very shallow, resulting in the CG algorithm failing to converge for nearly every MOF-adsorbate system studied in this work. The FIRE algorithm, which is a molecular dynamics method, was found to reach convergence in these otherwise problematic cases. This is consistent with the findings of Bitzek et al.[70] who demonstrated that the FIRE algorithm is both more efficient and robust than the typical CG and QN schemes when the forces are sufficiently low. For this reason, we also switch to the FIRE algorithm in any other part of the HT-DFT workflow if the default CG algorithm fails. The key DFT parameters are summarized in Table 2 (with all parameters listed in Table S2).

Table 2. Periodic DFT parameters used in the optimizing MOFs with adsorbates. ENCUT is the plane-wave kinetic energy cutoff, KPPA is the number of k-points per atom (with the corresponding k-point grids generated using Pymatgen[1]), and $|F_{\text{max}}|$ is the force-convergence criterion.

Stage	ENCUT (eV)	KPPA	$\lvert F_{\text{max}}\rvert$ (eV/Å)
1: Ionic relaxation	400	100	0.05

(low-accuracy)			
2: Ionic relaxation (medium-accuracy)	400	1000	0.05
3: Ionic relaxation (high-accuracy)	520	1000	0.03
4: Single-point (high-accuracy)	520	1000	N/A

Figure 7a and 7b emphasize the value in using a multi-stage workflow, as the lower accuracy runs often result in nearly converged geometries and therefore greatly accelerate the HT-DFT workflow. Since energy differences are typically desired for catalytic applications, we also computed the H-affinity previously shown in Equation (1) at the low-, medium-, and high-accuracy settings. Similar to what was shown in Figure 5, the results in Figure 7c emphasize the need to use 1000 KPPA over the much coarser 100 KPPA k-point density. However, as shown in Figure 7d, the increase in cutoff from 400 eV to 520 eV (and tighter force-convergence of $|F_{\mathrm{max}}| < 0.03$ eV/ Å compared to 0.05 eV/Å) does not significantly change the computed H-affinity beyond 1−2 kJ/mol on average, which is far below the expected accuracy from the choice of exchange-correlation functional and any TS scaling relationships. That being said, due to the nearly converged geometry at the end of the medium-accuracy run, the high-accuracy calculations exhibit rapid convergence (particularly when starting from the previously converged wavefunctions), so we decided to still include this step in the workflow.

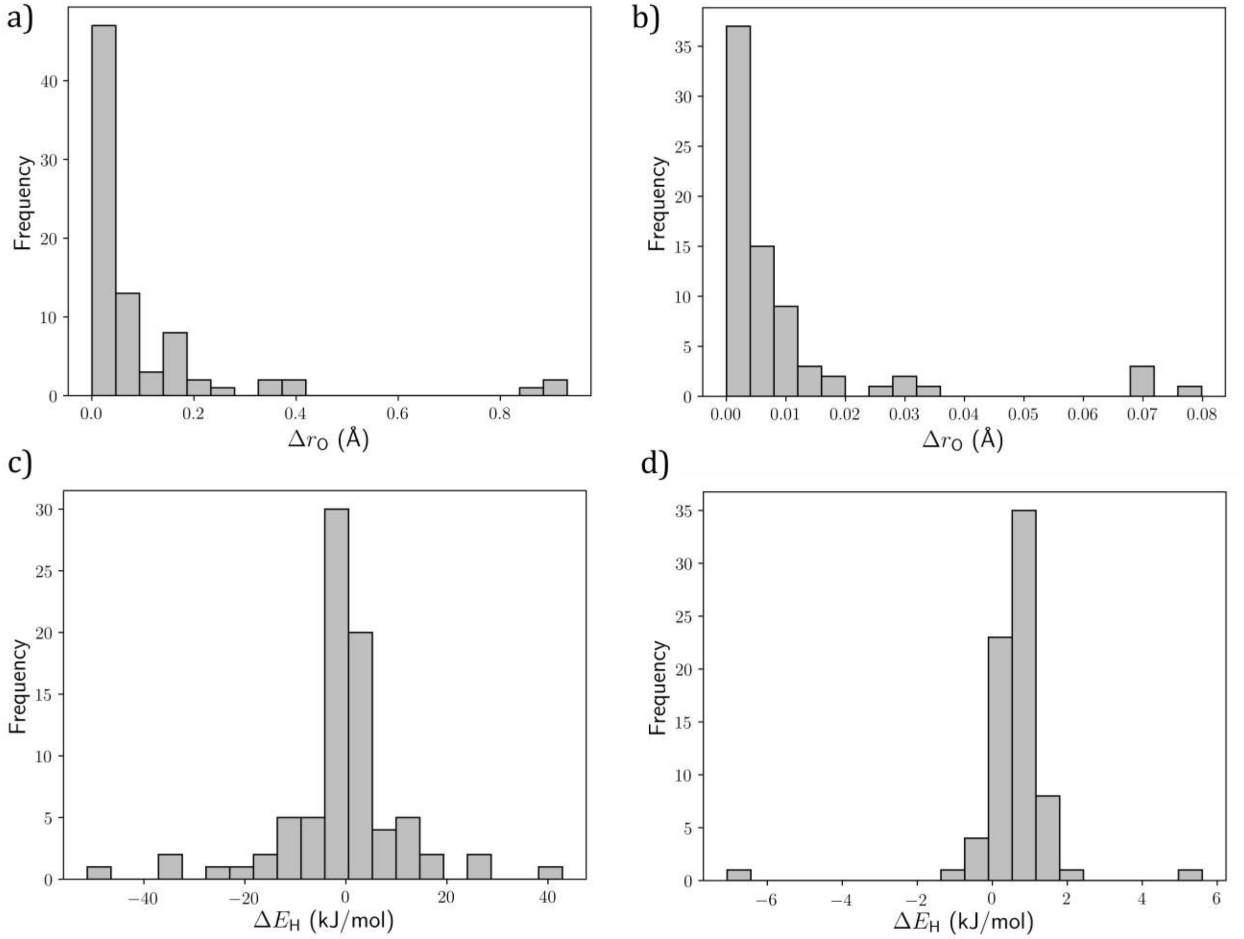

Figure 7. (a) Deviation in the position of the O adsorbate, Δr_{O}, for the formation of the active site between the low-accuracy and medium-accuracy run. (b) Deviation in Δr_{O} between the medium-accuracy and high-accuracy run. (c) Deviation in H-affinity, ΔE_{H}, computed with low-accuracy settings (cutoff = 400 eV, KPPA = 100, $|F_{\mathrm{max}}| < 0.05$ eV/Å) compared to medium-accuracy settings (cutoff = 400 eV, KPPA = 1000, $|F_{\mathrm{max}}| < 0.05$ eV/Å), defined as $\Delta E_{\mathrm{H}} = E_{\mathrm{H,med\ acc.}} - E_{\mathrm{H,low\ acc.}}$. (d) ΔE_{H} computed with medium-accuracy settings and high-accuracy settings (cutoff = 520 eV, KPPA = 1000, $|F_{\mathrm{max}}| < 0.03$ eV/Å), defined as $\Delta E_{\mathrm{H}} = E_{\mathrm{H,high\ acc.}} - E_{\mathrm{H,med\ acc.}}$.

6.4 Spin-Polarization

To account for spin-polarization, both high-spin and low-spin initial magnetic moments are considered in a procedure motivated in part by the Materials Project[8,9] and OQMD.[7] In the high-spin case, d-block elements (i.e. Sc−Cu, Y−Ag, Hf−Au) are initialized in a high-spin state of 5 μ_{B} (Bohr magnetons), all f-block elements (i.e. La−Lu, Ac−Lr) are initialized with 7 μ_{B}, all metals and semi-metals in groups 12−17 are initialized with 0.1 μ_{B}, and all s- and p-block metals are initialized with no spin. Once the high-spin run is completed, if the absolute values of the converged magnetic moment for each atom is less than 0.1 μ_{B} (or if there were no d- or f-block metals in the MOF), a low-spin configuration is not performed. Otherwise, a low-spin initial configuration is applied to the converged structure from the high-spin initialization, and the structure is reoptimized. For the low-spin case, the only difference is that the d- and f-block elements are initialized with 0.1 μ_{B} instead of 5 μ_{B} and 7 μ_{B}, respectively. If at the end of any step of the HT-DFT workflow the low-spin calculation converges to the magnetic moments that resulted from the high-spin calculation, the low-spin calculation is aborted. Two spin states are deemed to be equal if the converged magnetic moments are all within ±0.05 μ_B. While the high-spin initialization is sufficient for many of the MOFs studied in this work, the low-spin initialization can result in significantly more stable structures for select MOFs, as shown in Figure 8. Benchmarking of this spin treatment is shown in Table S3 and indicates that it is often sufficient for determining low-energy spin states, especially for the purposes of HT screening. Additional details regarding the convergence to complex magnetic orderings, such as antiferromagnetism, are discussed in the Supporting Information.

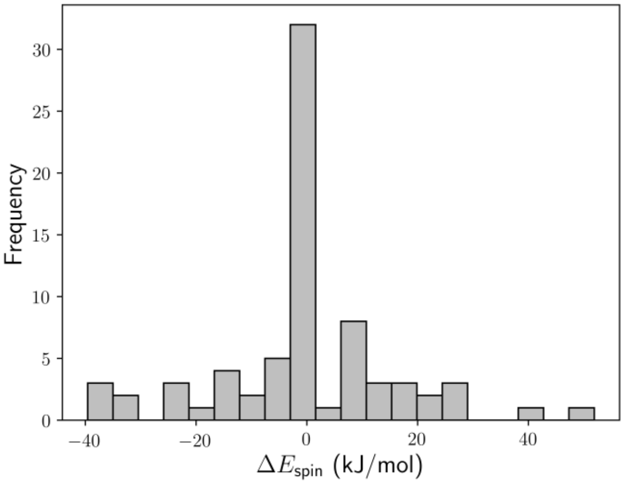

Figure 8. Difference in energy between the converged high-spin and low-spin electronic energies, $\Delta E_\mathrm{spin} = E_\mathrm{high\ spin} - E_\mathrm{low\ spin}$, of MOFs where a full low-spin calculation was performed.

6.5 Implementation of Methods

Additional details regarding the implementation of the periodic DFT screening workflow used in this study can be found in the Supporting Information. An open-source Python code referred to as PyMOFScreen is made publicly available to readily perform fully automated periodic DFT calculations of MOFs using the related workflows to those described in this work.[72] As with the MOF Adsorbate Initializer, PyMOFScreen makes extensive use of Pymatgen[1] and ASE[2] to set up and carry out the DFT calculations. We note that analogous workflows could be readily constructed using the highly flexible Atomate package as well.[4]

7. Oxidative C-H Bond Activation

With the developed HT screening workflow, we identified MOFs in an 838 MOF subset of the CoRE MOF database[44] that contained OMSs (Section 4), performed volume relaxations on each MOF (Section 6), initialized the positions of relevant adsorbates (Section 5), and performed ionic relaxations on each MOF with bound adsorbates to calculate adsorption energies (Section 6). The volume relaxation (i.e. E_MOF) and three ionic relaxations (i.e. $E_\mathrm{MOF-O}$, $E_\mathrm{MOF-OH}$, $E_\mathrm{MOF-O-CH_4}$) all achieved 99−100% convergence of the screened MOFs in this work, indicative of the robustness of the developed HT-DFT workflow. With the DFT-computed adsorption energies, we subsequently used Equations (1)−(4) to calculate the catalytic descriptors of interest. The results of the catalytic screening for oxidative C-H bond activation of methane are discussed below.

As shown in Figure 9a, the vast majority of screened MOFs have strongly endothermic oxidation reaction energies in the presence of an N_2O oxidant. Thermodynamically, this suggests that there will only be a small (potentially negligible) population of metal-oxo active sites present at moderate reaction conditions. Kinetically, since the lower-bound for the activation barrier is set by the reaction energy for endothermic reactions, this also implies that the rate of N_2O activation is likely to be very low. As a result of this phenomenon, we expect that few MOFs in the 838 CoRE MOF subset have accessible metal sites that can be readily oxidized using N_2O.

Nonetheless, it is clear from Figure 9b that if a metal-oxo active site can be formed, the barrier for C-H activation would likely be sufficiently low for the catalytic conversion of methane for most MOFs considered in this work, as every MOF tested in this study has a methane C-H activation barrier below 100 kJ/mol, comparable to many cation-exchanged zeolites that can activate methane.[73] It is common in the computational catalysis literature to focus on the C-H activation step due to the large 440 kJ/mol bond dissociation energy of methane (when not in the presence of a catalyst).[74] However, the results shown in Figure 9 suggest that the main challenge in terms of high-throughput screening is not identifying MOFs with low C-H activation barriers, but rather identifying MOFs with OMSs that can be readily oxidized. Indeed, despite the many thousands of MOFs that have been synthesized to date, there are relatively few that have been experimentally shown to exhibit redox-active OMSs for catalytic applications.[23]

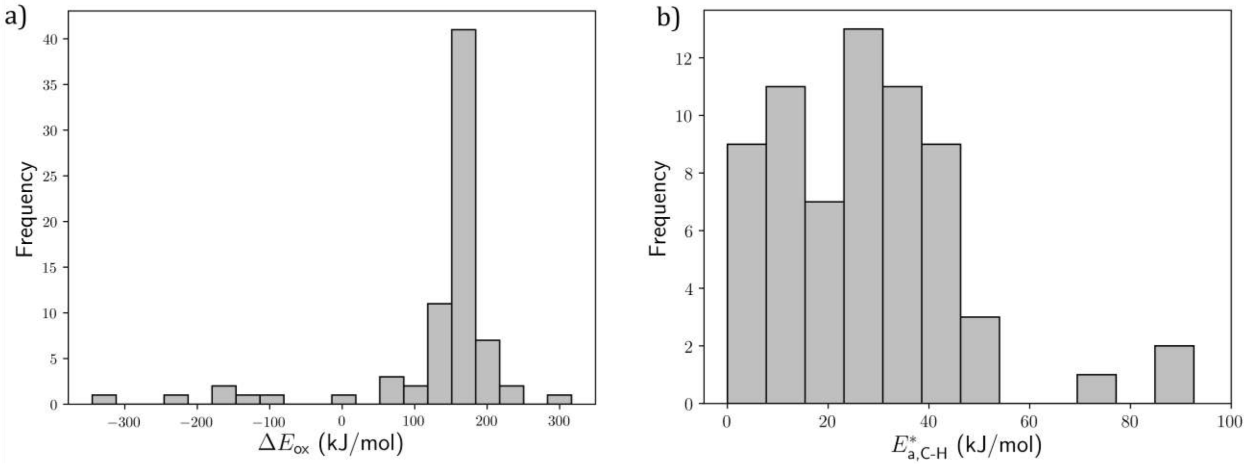

Figure 9. (a) Reaction energy for N_2O activation, ΔE_{ox}, defined in Equation (4). (b) Methane C-H activation barrier at metal oxide active site, $E^*_{\mathrm{a,C-H}}$, defined in Equation (3).

As one example from the HT-DFT analysis, consider $Cu_3(dmtrz)_2(ox)_2$ (Hdmtrz = 3,5-dimethyl-1H-1,2,4-triazole, ox = oxalate, CSD refcode = LIFWEE)[75] shown in Figure 10. The structure of $Cu_3(dmtrz)_2(ox)_2$ has mono(μ-aquo) Cu(II,II) dimers that can be desolvated around 125 °C, leaving behind adjacent square-planar Cu(II) sites.[75] In principle, the dicopper(II) species can be oxidized to form mono(μ-oxo) dicopper(III) species. This mono(μ-oxo) dicopper(III) species is extremely active toward the C-H activation of methane, with a predicted barrier of $E^*_{\mathrm{a,C-H}} = 40$ kJ/mol. Despite this high reactivity toward H-abstraction, it can be expected that

$Cu_3(dmtrz)_2(ox)_2$ would not be promising for oxidative C-H bond activation, as the computed reaction energy for formation of the mono(μ-oxo) dicopper(III) species is strongly endothermic ($\Delta E_{\mathrm{ox}} = 127$ kJ/mol).

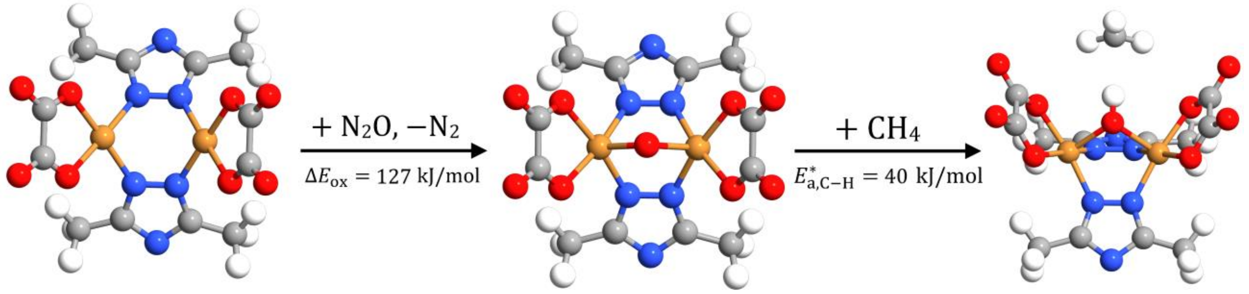

Figure 10. Formation of the metal oxide active site and subsequent H-abstraction of methane with $Cu_3(dmtrz)_2(ox)_2$. Color key: Cu (orange), C (gray), N (blue), O (red), H (white). Structures are DFT-optimized (only a representative portion of the unit cell is shown for clarity).

One approach to increase the likelihood of accessing low C-H bond activation barriers with MOFs containing OMSs is to increase the temperature during the oxidation step. This is a common and often necessary approach in the Cu-exchanged zeolite literature, where a multi-step conversion process is performed with O_2 or N_2O activation around 450 °C and subsequent methane activation around 125–200 °C.[76–79] However, applying this approach to most MOFs is likely to be challenging, as the majority of MOFs are not capable of withstanding harsh thermal treatment without significant decomposition of the framework, especially in the presence of air or other oxidizing agents.[80] One of the more thermally and chemically stable MOFs synthesized to date is $Ni_3(BTP)_2$ (H_3BTP = 1,3,5-tris(1*H*-pyrazol-4-yl)benzene, CSD refcode = UTEWOG),[81] which is stable in air up to 430 °C and is included in the database of MOFs screened in this work (its structure was previously shown in Figure 3). From the present work, we predict that $E^*_{\mathrm{a,C-H}} = 25$ kJ/mol. However, we also predict that $\Delta E_{\mathrm{ox}} = 119$ kJ/mol, which is likely to prevent sufficient oxidation of the metal site even at elevated temperatures near the stability limit of $Ni_3(BTP)_2$.

Another general approach to increase the activity of MOFs for oxidative C-H bond activation when N_2O activation is the rate-limiting step is to consider the use of a more reactive oxidizing agent. As one example, H_2O_2 could be used and would act as a green oxidant since it only releases water as the byproduct. In addition to being more kinetically reactive than N_2O, the standard enthalpy of reaction for MOF + $H_2O_2 \rightarrow$ MOF−O + H_2O compared to MOF + $N_2O \rightarrow$ MOF−O + N_2 is more thermodynamically favorable by 82 kJ/mol at the PB3-D3(BJ) level of theory. H_2O_2 has recently been used as the oxidant in the conversion of methane to methanol with Fe-containing Al-MIL-53[31,82] as well as graphene-confined single Fe atoms[83] and multiple works involving cation-exchanged zeolites[25,84,85]. The use of other strong oxidizing agents is also likely worth considering for the purposes of gaining experimental insight into oxidative C-H bond activation on MOF-supported metal-oxo species. For instance, the strong oxidant $K_2S_2O_8$ has been used for the conversion of methane to acetic acid with V-containing MIL-47 and MOF-48 catalysts.[28] Although the most industrially desirable oxidant is air or O_2, the use of strong oxidants is expected to significantly aid experimental investigation of MOFs capable of activating the strong C-H bond of methane.

While seven MOF structures were identified as having exothermic ΔE_{ox} values, they are unlikely to be experimentally realizable, as they have unexpected structural defects or solvents that are unlikely to be removed. These instances can often be traced back to challenges in experimentally resolving the positions of ligands or charge-balancing ions during X-ray diffraction studies and/or their removal in construction of the CoRE MOF database. As an example, we highlight one MOF with a predicted exothermic oxidation reaction energy but an ambiguous crystal structure. This MOF, referred to as Rh-BMOF-1 (B = 4,4'-bipyridine, CSD refcode = TERFUT), is a post-synthetically modified, cyclometalated MOF obtained from the reaction of a Rh(I) precursor and a 2-phenylpyridine-5,4'-dicarboxylic acid (dcppy) ligand.[86] BMOF-1 and the related DMOF-1 (D = DABCO = 1,4-diazabicyclo[2.2.2]octane) can be synthesized with Rh(I) or Ir(I) species anchored between a carbanion and a nitrogen atom of the nearby pyridine in the dcppy ligand.[86] Rh-BMOF-1 is predicted to have $\Delta E_{\text{ox}} = -153$ kJ/mol and $E^*_{\text{a,C-H}} = 91$ kJ/mol when using the as-published crystal structure with two-coordinate Rh(I) cations.

It is likely that the highly exothermic ΔE_{ox} value can be attributed to atypically undercoordinated Rh(I) sites. Since Rh(I) and Ir(I) are d^8 metals, it is more likely that they form square-planar geometries via the coordination of two additional ligands, as has been found in a related Rh(I)-containing MOF by Sumby and coworkers.[87] As an example, the presence of CO or CH_3CN ligands greatly reduces the redox activity of the Rh(I) and Ir(I) sites, although the resulting C-H activation barrier is expected to be lower if the active site were to form (Figure 11). Since the exact nature of the bound ligands has not been experimentally determined due to low occupancies of the cyclometalated species in the crystal structure,[86] we focus on other screened MOFs for the remainder of the analysis.

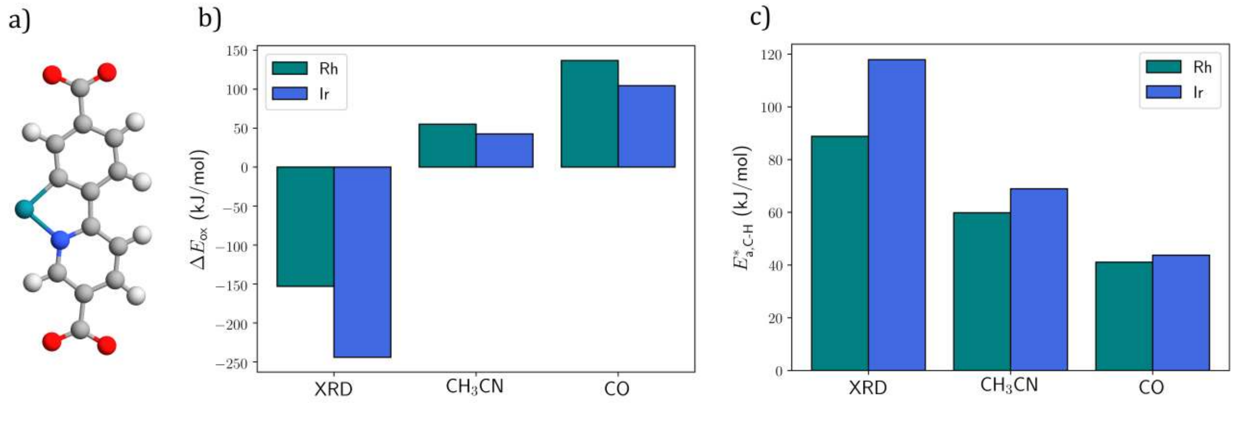

Figure 11. (a) Rh(I) environment in cyclometalated DMOF-1 based on the structure from X-ray diffraction (XRD) (i.e. no additional ligands). The structure is DFT-optimized (only a representative portion of the unit cell is shown for clarity). Color key: Rh (teal), C (gray), N (blue), O (red), H (white). (b) Extrinsic reaction energy for oxidation via N_2O, ΔE_{ox}, defined in Equation (4). (c) Methane C-H activation barrier, $E^*_{\text{a,C-H}}$, at metal oxide active sites, defined in Equation (3). XRD, CH_3CN, and CO refer to the two-coordinate metal, square-planar metal environment with two CH_3CN ligands, and square-planar metal environment with two CO ligands. Energetics are identical for the interpenetrated BMOF-1.

From the HT-DFT procedure, the MOF with the lowest oxidation reaction energy and a fully resolved crystal structure is $Cu_8I_4(dmtrz)_4$ (CSD refcode = CUNFOH01), which contains Cu(I)-I cubane tetramers as well as two-coordinate Cu(I) cations,[88] of which only the latter are expected to be readily accessible for oxidation by N_2O. The HT-DFT analysis suggests that the two-coordinate Cu(I) sites in $Cu_8I_4(dmtrz)_4$ have $\Delta E_{\mathrm{ox}} = 103$ kJ/mol and $E^*_{\mathrm{a,C-H}} = 36$ kJ/mol. With the goal of identifying Cu(I) cations that can be more easily oxidized, we screened the 2019 CoRE MOF database[17] for MOFs with two-coordinate Cu(I) species, a PLD greater than 3.0 Å, and less than 400 atoms in the Niggli-reduced unit cell. From this procedure, we identified Cu_2(tqpt) (H_2tqpt = 6,6,14,14-tetramethyl-6,14-dihydroquin-oxalino-[2,3-*b*]phenazinebistriazole, CSD refcode = URUWEL), also known as CFA-8,[89] which has the topology shown in Figure 12a. CFA-8 contains two-coordinate (linear), three-coordinate (trigonal planar), and four-coordinate (tetrahedral) Cu(I) species in the framework. We will refer to these species as Cu_A, Cu_B, and Cu_C, respectively.

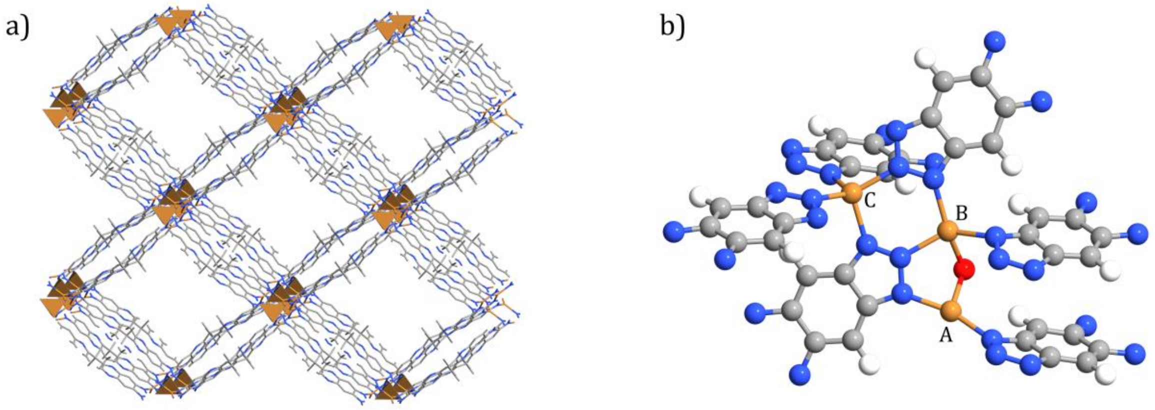

Figure 12. (a) Structure of CFA-8 with Cu(I) ions lining the pore along the c-axis. H atoms omitted for clarity. (b) Ball-and-stick model of distinct Cu sites in CFA-8 and a proposed mono(μ-oxo) dicopper(II) active site following activation of N_2O. Color key: Cu (orange), C (gray), N (blue), O (red), H (white). Structures are DFT-optimized.

Due to the close proximity of Cu(I) species in the framework, we hypothesized that the thermodynamics for oxidation via N_2O could be significantly more favorable than that of $Cu_8I_4(dmtrz)_4$ via the formation of a mono(μ-oxo) motif bridging two neighboring Cu(I) sites (Figure 12b). Based on the HT-DFT calculations, the extrinsic oxidation reaction energy is $\Delta E_{\mathrm{ox}} = 47$ kJ/mol, which is significantly more thermodynamically achievable than the other MOFs screened in this study. The proposed $[Cu_2O]^{2+}$ core of oxidized CFA-8 contains a bent geometry with a Cu_A-O-Cu_B bond angle of 103° and equal Cu_A-O and Cu_B-O bond lengths of 1.88 Å. The Cu_A-Cu_B bond length decreases from 3.40 Å in the bare MOF to 2.96 Å in the oxidized state.

The potential energy diagram of the proposed mechanism for oxidative C-H bond activation of methane in this MOF is shown in Figure 13. For the mono(μ-oxo) sites in CFA-8, we calculate that $E_{\mathrm{a,C-H}} = 57$ kJ/mol, which is essentially identical to the experimentally observed ~65 kJ/mol barrier attributed to similar mono(μ-oxo) dicopper(II) active sites in Cu-ZSM-5 that can catalytically convert methane to methanol.[76] It is also predicted that methanol, the desired product, should readily desorb at ambient conditions, which is commonly problematic for cation-exchanged zeolites.[90] We note that the barrier for N_2O activation to form the $[Cu_2O]^{2+}$ site is relatively high with a predicted value of 152 kJ/mol, such that it still expected to dictate the overall reaction kinetics for this system. Improved catalytic performance can potentially be achieved by considering more reactive oxidants. Provided a transient mono(μ-oxo) active site can be formed, CFA-8 would likely be a promising candidate for oxidative C-H bond activation reactions.

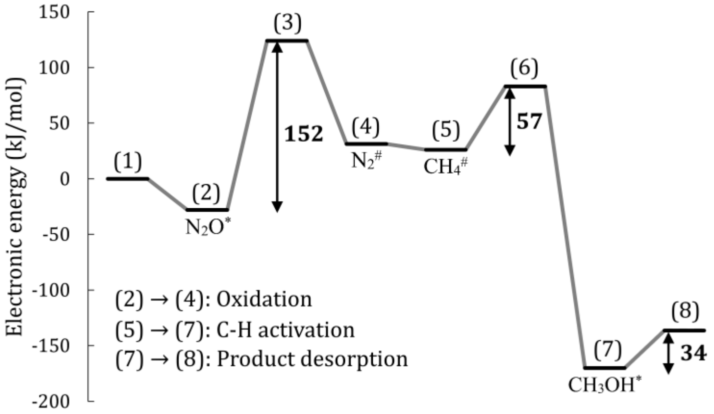

Figure 13. Potential energy diagram for oxidation of the metal centers via N_2O, subsequent H-abstraction of methane, and formation/desorption of methanol with CFA-8. (1) MOF + N_2O (g) + CH_4 (g); (2) N_2O^*; (3) transition state for N_2O activation; (4) $N_2^\#$; (5) $CH_4^\#$; (6) transition state for H-abstraction; (7) CH_3OH^*; (8) MOF + CH_3OH (g) + N_2 (g). Here, * denotes adsorption at the metal center and # denotes adsorption at the metal-oxo site formed via oxidation. Since the barrier for the radical rebound of •CH_3 is expected to be small compared to the other barriers, this step is omitted.

To obtain a better understanding of the proposed $[Cu_2O]^{2+}$ active site of CFA-8, we calculated the density-derived electrostatic and chemical (DDEC) partial atomic charges[91] and Bader spin density[92] for each atom. As shown in Table 3, the DDEC charges on the Cu(I) sites increase from 0.26 to 0.53–0.57 following N_2O activation. The large increase and near-equal magnitude of the partial atomic charges on the Cu species is consistent with the oxidation of the Cu(I) sites to mono(μ-oxo) dicopper(II) species. At the TS for N_2O activation, the DDEC analysis suggests that the Cu_B site is more easily oxidized than the Cu_A site, with the Cu_B site being almost entirely oxidized from Cu(I) to Cu(II) at the TS.

Formally, the H-abstraction from methane should decrease the charge of the active site by one. Instead of equally reducing the charge on both Cu(II) sites, the DDEC analysis indicates that the Cu_A site is more significantly reduced, whereas the Cu_B retains most of its charge. The Bader spin densities provide additional insight into this phenomenon. Since it is expected that a Cu(I) species should have no net spin, the Bader spin densities suggest that the Cu_A and Cu_B sites are likely best described as being in the 1+ and 2+ oxidation state following H-abstraction, respectively. The Bader spin density analysis also highlights the radical-like character of the bridging oxo species prior to H-abstraction, which results in the low methane C-H activation barrier of 57 kJ/mol. Finally, the formation of methanol closes the redox-cycle, with both the Cu_A and Cu_B sites returning to their original 1+ oxidation states.

Table 3. DDEC6 partial atomic charges[91] and Bader spin densitiy[92] for the proposed active site of CFA-8 throughout the radical-rebound mechanism. Cu_A and Cu_B refer to the Cu sites shown in Figure 12b. $S = 1$ and $S = 3$ refer to the closed-shell singlet and open-shell triplet spin multiplicities, respectively. $S = 1^*$ refers to an open-shell singlet state with an antiferromagnetic coupled methyl radical.

	Bare MOF	TS for formation of $[Cu_2O]^+$ site	Oxidized MOF	TS for C-H activation of CH_4	MOF with adsorbed $\bullet CH_3$	MOF with adsorbed CH_3OH
			DDEC partial atomic charge			
Cu_A	0.26	0.34	0.53	0.40	0.36	0.27
Cu_B	0.26	0.52	0.57	0.54	0.52	0.28
O	--	−0.50	−0.61	−0.65	−0.72	−0.45
			Magnitude of Bader spin density			
Cu_A			0.38	0.04	0.11	
Cu_B			0.48	0.33	0.40	
O			0.76	0.11	0.15	
			Spin multiplicity			
	$S = 1$	$S = 1$	$S = 3$	$S = 1^*$	$S = 1^*$	$S = 1$

8. Conclusions

High-throughput periodic DFT is a promising method for accelerating the discovery of MOFs for various applications, but there are numerous technical challenges that must be addressed before it can be routinely used to design and/or discover MOF candidates. In this work, we have developed a robust and automated workflow for the high-throughput screening of MOFs using periodic DFT, specifically focusing on applications in heterogeneous catalysis. We describe appropriate choices for electronic and structural optimization algorithms, treatment of spin states, and methods for automating the calculation of adsorption energies at open metal sites.

As a proof-of-concept, we applied this workflow to screen MOFs with open metal sites from an 838 MOF subset of the CoRE MOF database[16,44] for the oxidative C-H bond activation of methane using an N_2O oxidant. From this high-throughput procedure, it was found that oxidation of the metal – and not the C-H bond activation of methane – is the step with the largest barrier for the vast majority of screened MOFs in this work. Based on this finding, we expect that the development of new MOF datasets focused on low-valence, redox-active open metal sites will be central to the discovery of MOF-based heterogeneous catalysts that can directly convert methane to methanol at ambient conditions as well as other oxidative C-H bond activation reactions. While there are countless experimental studies of gas adsorption in MOFs, there are relatively few studies focusing on N_2O adsorption or activation,[93–97] so this serves as an avenue for further research as well. With the high-throughput framework outlined in this work, we hope that high-throughput periodic density functional theory will become a more mainstream tool for designing and identifying MOFs with unique physicochemical properties.

Acknowledgments

A.S.R. acknowledges government support under contract FA9550-11-C-0028 and awarded by the Department of Defense, Air Force Office of Scientific Research, National Defense Science and

Engineering Graduate (NDSEG) Fellowship, 32 CFR 168a. A.S.R. also gratefully acknowledges support from the Ryan Fellowship and the International Institute for Nanotechnology at Northwestern University. The material in this work is supported by the Institute for Catalysis in Energy Processes (ICEP) via the U.S. Department of Energy, Office of Science, Office of Basic Energy Sciences under Award Number DOE DE-FG02-03-ER15457. The authors acknowledge computing support through the resources and staff contributions provided for the Quest high-performance computing facility at Northwestern University as well as the Extreme Science and Engineering Discovery Environment (XSEDE)[98] via Stampede2 at the Texas Advanced Computing Center, which is supported by National Science Foundation grant number ACI-1548562. The authors acknowledge Benjamin Bucior for assistance with setting up the potential energy grid calculations, Arun Gopalan for assistance with visualizing the potential energy grids, and Hieu A. Doan for useful discussions regarding transition state scaling relations.

References

(1) Ong, S. P.; Richards, W. D.; Jain, A.; Hautier, G.; Kocher, M.; Cholia, S.; Gunter, D.; Chevrier, V. L.; Persson, K. A.; Ceder, G. Python Materials Genomics (Pymatgen): A Robust, Open-Source Python Library for Materials Analysis. *Comput. Mater. Sci.* **2013**, *68*, 314–319.

(2) Larsen, A.; Mortensen, J.; Blomqvist, J.; Castelli, I.; Christensen, R.; Dulak, M.; Friis, J.; Groves, M.; Hammer, B.; Hargus, C.; Hermes, E.; Jennings, P.; Jensen, P.; Kermode, J.; Kitchin, J.; Kolsbjerg, E.; Kubal, J.; Kaasbjerg, K.; Lysgaard, S.; Maronsson, J.; Maxson, T.; Olsen, T.; Pastewka, L.; Peterson, A.; Rostgaard, C.; Schiøtz, J.; Schütt, O.; Strange, M.; Thygesen, K.; Vegge, T.; Vilhelmsen, L.; Walter, M.; Zeng, Z.; Jacobsen, K. The Atomic Simulation Environment—A Python Library for Working with Atoms. *J. Phys. Condens. Matter* **2017**, *29*, 273002.

(3) Pizzi, G.; Cepellotti, A.; Sabatini, R.; Marzari, N.; Kozinsky, B. AiiDA: Automated Interactive Infrastructure and Database for Computational Science. *Comput. Mater. Sci.* **2016**, *111*, 218–230.

(4) Mathew, K.; Montoya, J. H.; Faghaninia, A.; Dwarakanath, S.; Aykol, M.; Tang, H.; Chu, I. heng; Smidt, T.; Bocklund, B.; Horton, M.; Dagdelen, J.; Wood, B.; Liu, Z. K.; Neaton, J.; Ong, S. P.; Persson, K.; Jain, A. Atomate: A High-Level Interface to Generate, Execute, and Analyze Computational Materials Science Workflows. *Comput. Mater. Sci.* **2017**, *139*, 140–152.

(5) Jain, A.; Ong, S. P.; Chen, W.; Medasani, B.; Qu, X.; Kocher, M.; Brafman, M.; Petretto, G.; Rignanese, G.-M.; Hautier, G.; Gunter, D.; Persson, K. FireWorks: A Dynamic Workflow System Designed for High-Throughput Applications. *Concurr. Comput. Pract. Exp.* **2015**, *27*, 5037–5059.

(6) Mayeshiba, T.; Wu, H.; Angsten, T.; Kaczmarowski, A.; Song, Z.; Jenness, G.; Xie, W.; Morgan, D. The MAterials Simulation Toolkit (MAST) for Atomistic Modeling of Defects and Diffusion. *Comput. Mater. Sci.* **2017**, *126*, 90–102.

(7) Saal, J. E.; Kirklin, S.; Aykol, M.; Meredig, B.; Wolverton, C. Materials Design and Discovery with High-Throughput Density Functional Theory: The Open Quantum Materials Database (OQMD). *Jom* **2013**, *65*, 1501–1509.

(8) Jain, A.; Ong, S. P.; Hautier, G.; Chen, W.; Richards, W. D.; Dacek, S.; Cholia, S.; Gunter, D.; Skinner, D.; Ceder, G.; Persson, K. A. The Materials Project: A Materials Genome Approach to Accelerating Materials Innovation. *APL Mater.* **2013**, *1*, 11002.

(9) Jain, A.; Hautier, G.; Moore, C. J.; Ping Ong, S.; Fischer, C. C.; Mueller, T.; Persson, K. A.; Ceder, G. A High-Throughput Infrastructure for Density Functional Theory Calculations. *Comput. Mater. Sci.* **2011**, *50*, 2295–2310.

(10) Curtarolo, S.; Setyawan, W.; Wang, S.; Xue, J.; Yang, K.; Taylor, R. H.; Nelson, L. J.; Hart, G. L. W.; Sanvito, S.; Buongiorno-Nardelli, M.; Mingo, N.; Levy, O. AFLOWLIB.ORG: A Distributed Materials Properties Repository from High-Throughput Ab Initio Calculations. *Comput. Mater. Sci.* **2012**, *58*, 227–235.

(11) Landis, D. D.; Hummelshoj, J. S.; Nestorov, S.; Greeley, J.; Dulak, M.; Bligaard, T.; Nørskov, J. K.; Jacobsen, K. W. The Computational Materials Repository. *Comput. Sci. Eng.* **2012**, *14*, 51–57.

(12) Choudhary, K.; Kalish, I.; Beams, R.; Tavazza, F. High-Throughput Identification and Characterization of Two-Dimensional Materials Using Density Functional Theory. *Sci. Rep.* **2017**, *7*, 1–16.

(13) Curtarolo, S.; Hart, G. L. W.; Nardelli, M. B.; Mingo, N.; Sanvito, S.; Levy, O. The High-Throughput Highway to Computational Materials Design. *Nat. Mater.* **2013**, *12*, 191.

(14) Wilmer, C. E.; Leaf, M.; Lee, C. Y.; Farha, O. K.; Hauser, B. G.; Hupp, J. T.; Snurr, R. Q. Large-Scale Screening of Hypothetical Metal−Organic Frameworks. *Nat. Chem.* **2012**, *4*, 83–89.

(15) Moghadam, P. Z.; Li, A.; Wiggin, S. B.; Tao, A.; Maloney, A. G. P.; Wood, P. A.; Ward, S. C.; Fairen-Jimenez, D. Development of a Cambridge Structural Database Subset: A Collection of Metal–Organic Frameworks for Past, Present, and Future. *Chem. Mater.* **2017**, *29*, 2618–2625.

(16) Chung, Y. G.; Camp, J.; Haranczyk, M.; Sikora, B. J.; Bury, W.; Krungleviciute, V.; Yildirim, T.; Farha, O. K.; Sholl, D. S.; Snurr, R. Q. Computation-Ready, Experimental Metal−Organic Frameworks: A Tool to Enable High-Throughput Screening of Nanoporous Crystals. *Chem. Mater.* **2014**, *26*, 6185–6192.

(17) Chung, Y. G.; Haldoupis, E.; Bucior, B. J.; Haranczyk, M.; Lee, S.; Zhang, H.; Vogiatzis, K. D.; Milisavljevic, M.; Ling, S.; Camp, J. S.; Slater, B.; Siepmann, J. I.; Sholl, D. S.; Snurr, R. Q. Advances, Updates, and Analytics for the Computation-Ready, Experimental Metal-Organic Framework Database: CoRE MOF 2019. (in preparation).

(18) Colón, Y. J.; Gómez-Gualdrón, D. A.; Snurr, R. Q. Topologically Guided, Automated Construction of Metal–Organic Frameworks and Their Evaluation for Energy-Related Applications. *Cryst. Growth Des.* **2017**, *17*, 5801–5810.

(19) Chung, Y. G.; Gómez-Gualdrón, D. A.; Li, P.; Leperi, K. T.; Deria, P.; Zhang, H.; Vermeulen, N. A.; Stoddart, J. F.; You, F.; Hupp, J. T.; Farha, O. K.; Snurr, R. Q. In Silico Discovery of Metal−Organic Frameworks for Precombustion CO_2 Capture Using a Genetic Algorithm. *Sci. Adv.* **2016**, *2*, e1600909.

(20) Gómez-Gualdrón, D. A.; Colón, Y. J.; Zhang, X.; Wang, T. C.; Chen, Y. S.; Hupp, J. T.; Yildirim, T.; Farha, O. K.; Zhang, J.; Snurr, R. Q. Evaluating Topologically Diverse Metal−Organic Frameworks for Cryo-Adsorbed Hydrogen Storage. *Energy Environ. Sci.* **2016**, *9*, 3279–3289.

(21) Moghadam, P. Z.; Islamoglu, T.; Goswami, S.; Exley, J.; Fantham, M.; Kaminski, C. F.; Snurr, R. Q.; Farha, O. K.; Fairen-Jimenez, D. Computer-Aided Discovery of a Metal–Organic Framework with Superior Oxygen Uptake. *Nat. Commun.* **2018**, *9*, 1378.

(22) Bernales, V.; Ortuño, M. A.; Truhlar, D. G.; Cramer, C. J.; Gagliardi, L. Computational Design of Functionalized Metal–Organic Framework Nodes for Catalysis. *ACS Cent. Sci.* **2017**, *4*, 5–19.

(23) D'Alessandro, D. M. Exploiting Redox Activity in Metal–Organic Frameworks: Concepts, Trends and Perspectives. *Chem. Commun.* **2016**, *52*, 8957–8971.

(24) Götl, F.; Michel, C.; Andrikopoulos, P. C.; Love, A. M.; Hafner, J.; Hermans, I.; Sautet, P. Computationally Exploring Confinement Effects in the Methane-to-Methanol Conversion over Iron-Oxo Centers in Zeolites. *ACS Catal.* **2016**, *6*, 8404–8409.

(25) Mahyuddin, M. H.; Staykov, A.; Shiota, Y.; Yoshizawa, K. Direct Conversion of Methane to Methanol by Metal-Exchanged ZSM-5 Zeolite (Metal = Fe, Co, Ni, Cu). *ACS Catal.* **2016**, *6*, 8321–8331.

(26) Horn, R.; Schlögl, R. Methane Activation by Heterogeneous Catalysis. *Catal. Letters* **2015**, *145*, 23–39.

(27) Wu, J.; Liu, M.; Hou, H. Metal−Organic Frameworks Based Materials as Heterogeneous Catalysts for C-H Bond Activation. *Chem. – A Eur. J.* (in press). DOI: doi.org/10.1002/chem.201804149.

(28) Phan, A.; Czaja, A. U.; Gándara, F.; Knobler, C. B.; Yaghi, O. M. Metal–Organic Frameworks of Vanadium as Catalysts for Conversion of Methane to Acetic Acid. *Inorg. Chem.* **2011**, *50*, 7388–7390.

(29) Ikuno, T.; Zheng, J.; Vjunov, A.; Sanchez-Sanchez, M.; Ortuño, M. A.; Pahls, D. R.; Fulton, J. L.; Camaioni, D. M.; Li, Z.; Ray, D.; Mehdi, B. L.; Browning, N. D.; Farha, O. K.; Hupp, J. T.; Cramer, C. J.; Gagliardi, L.; Lercher, J. A. Methane Oxidation to Methanol Catalyzed by Cu-Oxo Clusters Stabilized in NU-1000 Metal–Organic Framework. *J. Am. Chem. Soc.* **2017**, *139*, 10294–10301.

(30) Zhang, X.; Huang, Z.; Ferrandon, M.; Yang, D.; Robison, L.; Li, P.; Wang, T. C.; Delferro, M.; Farha, O. K. Catalytic Chemoselective Functionalization of Methane in a Metal–Organic Framework. *Nat. Catal.* **2018**, *1*, 356–362.

(31) Osadchii, D.; Olivos Suarez, A. I.; Szécsényi, Á.; Li, G.; Nasalevich, M. A.; Dugulan, A. I.; Serra-Crespo, P.; Hensen, E. J. M.; Veber, S. L.; Fedin, M. V; Sankar, G.; Pidko, E. A.; Gascon, J. Isolated Fe Sites in Metal−Organic Framework Catalyze the Direct Conversion of Methane to Methanol. *ACS Catal.* **2018**, *8*, 5542–5548.

(32) Baek, J.; Rungtaweevoranit, B.; Pei, X.; Park, M.; Fakra, S. C.; Liu, Y.-S.; Matheu, R.; Alshmimri, S. A.; Alshihri, S.; Trickett, C. A.; Somorjai, G. A.; Yaghi, O. M. Bioinspired Metal−Organic Framework Catalysts for Selective Methane Oxidation to Methanol. *J. Am. Chem. Soc.* (in press). DOI: doi.org/10.1021/jacs.8b11525.

(33) Greeley, J.; Nørskov, J. K. Large-Scale, Density Functional Theory-Based Screening of Alloys for Hydrogen Evolution. *Surf. Sci.* **2007**, *601*, 1590–1598.

(34) Nørskov, J. K.; Bligaard, T.; Rossmeisl, J.; Christensen, C. H. Towards the Computational Design of Solid Catalysts. *Nat. Chem.* **2009**, *1*, 37–46.

(35) Nørskov, J. K.; Studt, F.; Abild-Pedersen, F.; Bligaard, T. *Fundamental Concepts in Heterogeneous Catalysis*; John Wiley & Sons, 2014.

(36) Bray, J. M.; Schneider, W. F. First-Principles Thermodynamic Models in Heterogeneous

Catalysis. In *Computational Catalysis*; Asthagiri, A., Janik, M. J., Eds.; The Royal Society of Chemistry, 2014; pp 84–93.

(37) Wang, S.; Petzold, V.; Tripkovic, V.; Kleis, J.; Howalt, J. G.; Skulason, E.; Fernandez, E. M.; Hvolbæk, B.; Jones, G.; Toftelund, A.; Falsig, H.; Björketun, M.; Studt, F.; Abild-Pedersen, F.; Rossmeisl, J.; Nørskov, J. K.; Bligaard, T. Universal Transition State Scaling Relations for (de)Hydrogenation over Transition Metals. *Phys. Chem. Chem. Phys.* **2011**, *13*, 20760–20765.

(38) Latimer, A. A.; Kulkarni, A. R.; Aljama, H.; Montoya, J. H.; Yoo, J. S.; Tsai, C.; Abild-Pedersen, F.; Studt, F.; Nørskov, J. K. Understanding Trends in C–H Bond Activation in Heterogeneous Catalysis. *Nat. Mater.* **2016**, *16*, 225–229.

(39) Gani, T. Z. H.; Kulik, H. J. Understanding and Breaking Scaling Relations in Single-Site Catalysis: Methane-to-Methanol Conversion by Fe(IV)=O. *ACS Catal.* **2018**, *8*, 1–36.

(40) Liao, P.; Getman, R. B.; Snurr, R. Q. Optimizing Open Iron Sites in Metal−Organic Frameworks for Ethane Oxidation: A First-Principles Study. *ACS Appl. Mater. Interfaces* **2017**, *9*, 33484–33492.

(41) Zimmermann, N. E. R.; Horton, M. K.; Jain, A.; Haranczyk, M. Assessing Local Structure Motifs Using Order Parameters for Motif Recognition, Interstitial Identification, and Diffusion Path Characterization. *Front. Mater.* **2017**, *4*, 1–13.

(42) Willems, T. F.; Rycroft, C. H.; Kazi, M.; Meza, J. C.; Haranczyk, M. Algorithms and Tools for High-Throughput Geometry-Based Analysis of Crystalline Porous Materials. *Microporous Mesoporous Mater.* **2012**, *149*, 134–141.

(43) Latimer, A. A.; Aljama, H.; Kakekhani, A.; Yoo, J. S.; Kulkarni, A.; Tsai, C.; Garcia-Melchor, M.; Abild-Pedersen, F.; Nørskov, J. K. Mechanistic Insights into Heterogeneous Methane Activation. *Phys. Chem. Chem. Phys.* **2017**, *19*, 3575–3581.

(44) Nazarian, D.; Camp, J. S.; Chung, Y. G.; Snurr, R. Q.; Sholl, D. S. Large-Scale Refinement of Metal–Organic Framework Structures Using Density Functional Theory. *Chem. Mater.* **2017**, *29*, 2521–2528.

(45) Hutter, J.; Iannuzzi, M.; Schiffmann, F.; VandeVondele, J. CP2K: Atomistic Simulations of Condensed Matter Systems. *Wiley Interdiscip. Rev. Comput. Mol. Sci.* **2014**, *4*, 15–25.

(46) VandeVondele, J.; Krack, M.; Mohamed, F.; Parrinello, M.; Chassaing, T.; Hutter, J. Quickstep: Fast and Accurate Density Functional Calculations Using a Mixed Gaussian and Plane Waves Approach. *Comput. Phys. Commun.* **2005**, *167*, 103–128.

(47) Chui, S. S.-Y.; Lo, S. M.-F.; Charmant, J. P. H.; Orpen, A. G.; Williams, I. D. A Chemically Functionalizable Nanoporous Material $[Cu_3(TMA)_2(H_2O)_3]_N$. *Science* **1999**, *283*, 1148–1150.

(48) Vogiatzis, K. D.; Haldoupis, E.; Xiao, D. J.; Long, J. R.; Siepmann, J. I.; Gagliardi, L. Accelerated Computational Analysis of Metal−Organic Frameworks for Oxidation Catalysis. *J. Phys. Chem. C* **2016**, *120*, 18707–18712.

(49) Rosen, A. S.; Notestein, J. M.; Snurr, R. Q. MOF Adsorbate Initializer

https://doi.org/10.5281/zenodo.1451875.

(50) Martin, M. G.; Siepmann, J. I. Transferable Potentials for Phase Equilibria. 1. United-Atom Description of *n*-Alkanes. *J. Phys. Chem. B* **1998**, *102*, 2569–2577.

(51) Dubbeldam, D.; Calero, S.; Ellis, D. E.; Snurr, R. Q. RASPA: Molecular Simulation Software for Adsorption and Diffusion in Flexible Nanoporous Materials. *Mol. Simul.* **2016**, *42*, 81–101.

(52) Haldoupis, E. Open Metal Detector https://github.com/emmhald/open_metal_detector.

(53) PorousMaterials.jl https://doi.org/10.5281/zenodo.1400838.

(54) Kresse, G.; Furthmüller, J. Efficient Iterative Schemes for Ab Initio Total-Energy Calculations Using a Plane-Wave Basis Set. *Phys. Rev. B* **1996**, *54*, 11169–11186.

(55) Kresse, G.; Joubert, D. From Ultrasoft Pseudopotentials to the Projector Augmented-Wave Method. *Phys. Rev. B* **1999**, *59*, 1758–1775.

(56) Blöchl, P. E. Projector Augmented-Wave Method. *Phys. Rev. B* **1994**, *50*, 17953–17979.

(57) Perdew, J. P.; Burke, K.; Ernzerhof, M. Generalized Gradient Approximation Made Simple. *Phys. Rev. Lett.* **1996**, *77*, 3865–3868.

(58) Grimme, S.; Antony, J.; Ehrlich, S.; Krieg, H. A Consistent and Accurate Ab Initio Parametrization of Density Functional Dispersion Correction (DFT-D) for the 94 Elements H-Pu. *J. Chem. Phys.* **2010**, *132*, 154104.

(59) Grimme, S.; Ehrlich, S.; Goerigk, L. Effect of the Damping Function in Dispersion Corrected Density Functional Theory. *J. Comput. Chem.* **2011**, *32*, 1456–1465.

(60) Nazarian, D.; Ganesh, P.; Sholl, D. S. Benchmarking Density Functional Theory Predictions of Framework Structures and Properties in a Chemically Diverse Test Set of Metal−organic Frameworks. *J. Mater. Chem. A* **2015**, *3*, 22432–22440.

(61) Formalik, F.; Fischer, M.; Rogacka, J.; Firlej, L.; Kuchta, B. Benchmarking of GGA Density Functionals for Modeling Structures of Nanoporous, Rigid and Flexible MOFs. *J. Chem. Phys.* **2018**, *149*, 064110.

(62) Henkelman, G.; Uberuaga, B. P.; Jónsson, H. A Climbing Image Nudged Elastic Band Method for Finding Saddle Points and Minimum Energy Paths. *J. Chem. Phys.* **2000**, *113*, 9901–9904.

(63) Henkelman, G.; Jónsson, H. A Dimer Method for Finding Saddle Points on High Dimensional Potential Surfaces Using Only First Derivatives. *J. Chem. Phys.* **1999**, *111*, 7010–7022.

(64) Teter, M. P.; Payne, M. C.; Allan, D. C. Solution of Schrödinger's Equation for Large Systems. *Phys. Rev. B* **1989**, *40*, 12255–12263.

(65) Bylander, D. M.; Kleinman, L.; Lee, S. Self-Consistent Calculations of the Energy Bands and Bonding Properties of $B_{12}C_3$. *Phys. Rev. B* **1990**, *42*, 1394–1403.

(66) Pulay, P. Convergence Acceleration of Iterative Sequences. The Case of SCF Iteration.

Chem. Phys. Lett. **1980**, *73*, 393–398.

(67) Kresse, G.; Furthmüller, J. Efficiency of Ab-Initio Total Energy Calculations for Metals and Semiconductors Using a Plane-Wave Basis Set. *Comput. Mater. Sci.* **1996**, *6*, 15–50.

(68) Monkhorst, H. J.; Pack, J. D. Special Points for Brillouin-Zone Integrations. *Phys. Rev. B* **1976**, *13*, 5188–5192.

(69) Francis, G. P.; Payne, M. C. Finite Basis Set Corrections to Total Energy Pseudopotential Calculations. *J. Phys. Condens. Matter* **1990**, *2*, 4395.

(70) Bitzek, E.; Koskinen, P.; Gähler, F.; Moseler, M.; Gumbsch, P. Structural Relaxation Made Simple. *Phys. Rev. Lett.* **2006**, *97*, 170201.

(71) Henkelman, G. VTST Tools http://theory.cm.utexas.edu/vtsttools/index.html.

(72) Rosen, A. S.; Notestein, J. M.; Snurr, R. Q. PyMOFScreen https://doi.org/10.5281/zenodo.1451873.

(73) Kulkarni, A. R.; Zhao, Z.-J.; Siahrostami, S.; Nørskov, J. K.; Studt, F. Cation-Exchanged Zeolites for the Selective Oxidation of Methane to Methanol. *Catal. Sci. Technol.* **2018**, *8*, 114–123.

(74) Haynes, W. M. *CRC Handbook of Chemistry and Physics*, 98th ed.; CRC Press: Boca Raton, FL, 2017.

(75) Ling, Y.; Zhang, L.; Li, J.; Du, M. A Robust Porous PtS-Type Cu(II) Metal–organic Framework: Single-Crystal-to-Single-Crystal Transformation with Reversible Guest Intercalation Accompanied by Colour Change. *CrystEngComm* **2011**, *13*, 768–770.

(76) Woertink, J. S.; Smeets, P. J.; Groothaert, M. H.; Vance, M. A.; Sels, B. F.; Schoonheydt, R. A.; Solomon, E. I. A $[Cu_2O]^{2+}$ Core in Cu-ZSM-5, the Active Site in the Oxidation of Methane to Methanol. *Proc. Natl. Acad. Sci.* **2009**, *106*, 18908–18913.

(77) Grundner, S.; Markovits, M. A. C.; Li, G.; Tromp, M.; Pidko, E. A.; Hensen, E. J. M.; Jentys, A.; Sanchez-Sanchez, M.; Lercher, J. A. Single-Site Trinuclear Copper Oxygen Clusters in Mordenite for Selective Conversion of Methane to Methanol. *Nat. Commun.* **2015**, *6*, 7546.

(78) Smeets, P. J.; Hadt, R. G.; Woertink, J. S.; Vanelderen, P.; Schoonheydt, R. A.; Sels, B. F.; Solomon, E. I. Oxygen Precursor to the Reactive Intermediate in Methanol Synthesis by Cu-ZSM-5. *J. Am. Chem. Soc.* **2010**, *132*, 14736–14738.

(79) Tomkins, P.; Ranocchiari, M.; Van Bokhoven, J. A. Direct Conversion of Methane to Methanol under Mild Conditions over Cu-Zeolites and Beyond. *Acc. Chem. Res.* **2017**, *50*, 418–425.

(80) Howarth, A. J.; Liu, Y.; Li, P.; Li, Z.; Wang, T. C.; Hupp, J. T.; Farha, O. K. Chemical, Thermal and Mechanical Stabilities of Metal−Organic Frameworks. *Nat. Rev. Mater.* **2016**, *1*, 15018.

(81) Colombo, V.; Galli, S.; Choi, H. J.; Han, G. D.; Maspero, A.; Palmisano, G.; Masciocchi, N.; Long, J. R. High Thermal and Chemical Stability in Pyrazolate-Bridged

Metal−Organic Frameworks with Exposed Metal Sites. *Chem. Sci.* **2011**, *2*, 1311–1319.

(82) Szécsényi, Á.; Li, G.; Gascon, J.; Pidko, E. A. Unraveling Reaction Networks behind the Catalytic Oxidation of Methane with H_2O_2 over a Mixed-Metal MIL-53 (Al, Fe) MOF Catalyst. *Chem. Sci.* **2018**, *9*, 6765–6773.

(83) Cui, X.; Li, H.; Wang, Y.; Hu, Y.; Hua, L.; Li, H.; Han, X.; Liu, Q.; Yang, F.; He, L.; Chen, X.; Li, Q.; Xiao, J.; Deng, D.; Bao, X. Room-Temperature Methane Conversion by Graphene-Confined Single Iron Atoms. *Chem* **2018**, 1–9.

(84) Xu, J.; Armstrong, R. D.; Shaw, G.; Dummer, N. F.; Freakley, S. J.; Taylor, S. H.; Hutchings, G. J. Continuous Selective Oxidation of Methane to Methanol over Cu-and Fe-Modified ZSM-5 Catalysts in a Flow Reactor. *Catal. Today* **2016**, *270*, 93–100.

(85) Hammond, C.; Forde, M. M.; Ab Rahim, M. H.; Thetford, A.; He, Q.; Jenkins, R. L.; Dimitratos, N.; Lopez-Sanchez, J. A.; Dummer, N. F.; Murphy, D. M.; Carley, A. F.; Taylor, S. H.; Willock, D. J.; Stangland, E. E.; Kang, J.; Hagen, H.; Kiely, C. J.; Hutchings, G. J. Direct Catalytic Conversion of Methane to Methanol in an Aqueous Medium by Using Copper-Promoted Fe-ZSM-5. *Angew. Chemie Int. Ed.* **2012**, *51*, 5129–5133.

(86) Dau, P. V; Kim, M.; Cohen, S. M. Site-Selective Cyclometalation of a Metal–organic Framework. *Chem. Sci.* **2013**, *4*, 601–605.

(87) Bloch, W. M.; Burgun, A.; Coghlan, C. J.; Lee, R.; Coote, M. L.; Doonan, C. J.; Sumby, C. J. Capturing Snapshots of Post-Synthetic Metallation Chemistry in Metal−organic Frameworks. *Nat. Chem.* **2014**, *6*, 906.

(88) Tzeng, B.-C.; Chang, T.-Y. Toward Copper (I)-Iodide-Based Coordination Architectures via N,N′-Bis(Pyridylcarbonyl)-4,4′-Diaminodiphenyl Ether with Different Solvent Compositions. *Cryst. Growth Des.* **2009**, *9*, 5343–5350.

(89) Schmieder, P.; Denysenko, D.; Grzywa, M.; Magdysyuk, O.; Volkmer, D. A Structurally Flexible Triazolate-Based Metal−Organic Framework Featuring Coordinatively Unsaturated Copper(I) Sites. *Dalt. Trans.* **2016**, *45*, 13853–13862.

(90) Dinh, K. T.; Sullivan, M. M.; Serna, P.; Meyer, R. J.; Dincă, M.; Román-Leshkov, Y. Viewpoint on the Partial Oxidation of Methane to Methanol Using Cu- and Fe-Exchanged Zeolites. *ACS Catal.* **2018**, *8*, 8306–8313.

(91) Manz, T. A.; Limas, N. G. Introducing DDEC6 Atomic Population Analysis: Part 1. Charge Partitioning Theory and Methodology. *RSC Adv.* **2016**, *6*, 47771–47801.

(92) Tang, W.; Sanville, E.; Henkelman, G. A Grid-Based Bader Analysis Algorithm without Lattice Bias. *J. Phys. Condens. Matter* **2009**, *21*, 84204.

(93) Saha, D.; Bao, Z.; Jia, F.; Deng, S. Adsorption of CO_2, CH_4, N_2O, and N_2 on MOF-5, MOF-177, and Zeolite 5A. *Environ. Sci. Technol.* **2010**, *44*, 1820–1826.

(94) Denysenko, D.; Jelic, J.; Magdysyuk, O. V; Reuter, K.; Volkmer, D. Elucidating Lewis Acidity of Metal Sites in MFU-4*l* Metal–Organic Frameworks: N_2O and CO_2 Adsorption in MFU-4*l*, Cu^I-MFU-4*l* and Li-MFU-4*L*. *Microporous Mesoporous Mater.* **2015**, *216*,

146–150.

(95) Xiao, D. J.; Bloch, E. D.; Mason, J. A.; Queen, W. L.; Hudson, M. R.; Planas, N.; Borycz, J.; Dzubak, A. L.; Verma, P.; Lee, K.; Bonino, F.; Crocellà, V.; Yano, J.; Bordiga, S.; Truhlar, D. G.; Gagliardi, L.; Brown, C. M.; Long, J. Oxidation of Ethane to Ethanol by N_2O in a Metal−Organic Framework with Coordinatively Unsaturated Iron(II) Sites. *Nat. Chem.* **2014**, *6*, 590–595.

(96) Yang, J.; Du, B.; Liu, J.; Krishna, R.; Zhang, F.; Zhou, W.; Wang, Y.; Li, J.; Chen, B. MIL-100Cr with Open Cr Sites for a Record N_2O Capture. *Chem. Commun.* **2018**.

(97) Ketrat, S.; Maihom, T.; Wannakao, S.; Probst, M.; Nokbin, S.; Limtrakul, J. Coordinatively Unsaturated Metal−Organic Frameworks $M_3(BTC)_2$ (M = Cr, Fe, Co, Ni, Cu, and Zn) Catalyzing the Oxidation of CO by N_2O: Insight from DFT Calculations. *Inorg. Chem.* **2017**, *56*, 14005–14012.

(98) Towns, J.; Cockerill, T.; Dahan, M.; Foster, I.; Gaither, K.; Grimshaw, A.; Hazlewood, V.; Lathrop, S.; Lifka, D.; Peterson, G. D.; Roskies, R.; Scott, J. R.; Wilkins-Diehr, N. XSEDE: Accelerating Scientific Discovery. *Comput. Sci. Eng.* **2014**, *16*, 62–74.